All-Wood Composite Material by Partial Fiber Surface Dissolution with an Ionic Liquid

Khakalo, Alexey

2019-02-04

Khakalo , A , Tanaka , A , Korpela , A , Hauru , L K J & Orelma , H 2019 , ' All-Wood Composite Material by Partial Fiber Surface Dissolution with an Ionic Liquid ' , ACS Sustainable Chemistry & Engineering , vol. 7 , no. 3 , pp. 3195-3202 . https://doi.org/10.1021/acssuschemeng.8b050

http://hdl.handle.net/10138/310617
https://doi.org/10.1021/acssuschemeng.8b05059

ACS EARTH AND SPACE CHEMISTRY

Article

Cite This: ACS Earth Space Chem. 2019, 3, 652−662

http://pubs.acs.org/journal/aesccq

Radiation Damage Effects in Chlorite Investigated Using Microfocus Synchrotron Techniques

William R. Bower,*[,†,‡,§,∥,○] Carolyn I. Pearce,[‡,§,∥,#] Andrew D. Smith,[§] Simon. M. Pimblott,[‡,§,∥,▽] J. Frederick W. Mosselmans,[⊥] and Richard A. D. Pattrick[†,‡]

[†]Research Centre for Radwaste Disposal, School of Earth and Environmental Science, The University of Manchester, Manchester M13 9PL, United Kingdom

[‡]Dalton Nuclear Institute, The University of Manchester, Manchester M13 9PL, United Kingdom

[§]Dalton Cumbrian Facility, Westlakes Science and Technology Park, Moor Row CA24 3HA, United Kingdom

[∥]Centre for Radiochemistry Research, School of Chemistry, The University of Manchester, Manchester M13 9PL, United Kingdom

[⊥]Diamond Light Source, Harwell, Oxfordshire OX11 0QX, United Kingdom

ABSTRACT: A detailed understanding of the mechanisms and effects of radiation damage in phyllosilicate minerals is a necessary component of the evaluation of the safety case for a deep geological disposal facility (GDF) for radioactive waste. Structural and chemical changes induced by α-particle damage will affect the performance of these minerals as reactive barrier materials (both in the near and far-field) over time scales relevant to GDF integrity. In this study, two examples of chlorite group minerals have been irradiated at α-particle doses comparable to those predicted to be experienced by the clay buffer material surrounding high-level radioactive waste canisters. Crystallographic aberrations induced by the focused $^4He^{2+}$ ion beam are revealed via high-resolution, microfocus X-ray diffraction mapping. Interlayer collapse by up to 0.5 Å is prevalent across both macrocrystalline and microcrystalline samples, with the macrocrystalline specimen displaying a breakdown of the phyllosilicate structure into loosely connected, multioriented crystallites displaying variable lattice parameters. The damaged lattice parameters suggest a localized breakdown and collapse of the OH^- rich, "brucite-like" interlayer. Microfocus Fe *K*-edge X-ray absorption spectroscopy illustrates this defect accumulation, manifest as a severe damping of the X-ray absorption edge. Subtle Fe^{2+}/Fe^{3+} speciation changes are apparent across the damaged structures. A trend toward Fe reduction is evident at depth in the damaged structures at certain doses (8.76×10^{15} alpha particles/cm^2). Interestingly, this reductive trend does not increase with radiation dose; indeed, at the maximum dose (1.26×10^{16} α particles/cm^2) administered in this study, there is evidence for a slight increase in Fe binding energy, suggesting the development of a depth-dependent redox gradient concurrent with light ion damage. At the doses examined here, these damaged structures are likely highly reactive, as sorption capacity will, to an extent, be largely enhanced by lattice disruption and an increase in available "edge" sites.

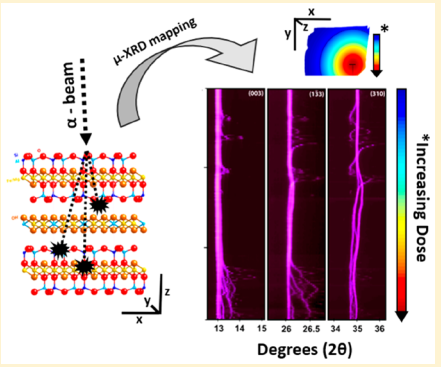

KEYWORDS: *chlorite, radiation damage, α particles, geodisposal, bentonite, montmorillonite, synchrotron microfocus, radioactive waste*

1. INTRODUCTION

Phyllosilicate minerals will have a key role in the safe geological isolation of nuclear waste[1,2] and their behavior under repository conditions must be fully understood. Under the globally favored strategies to construct a deep geological disposal facility (GDF), bentonite (the collective term for naturally occurring clay consisting, dominantly, of montmorillonite ($Na_{0.2}Ca_{0.1}Al_2Si_4O_{10}(OH)_2(H_2O)_{10}$)) directly surrounding the waste canister will be one of the primary engineered "barriers" to limit radionuclide release into the environment.[3,4] In the far-field of a GDF, phyllosilicates (micas and clays) will be the most reactive components of the host rock, also acting as "sinks" for radionuclides following eventual canister breakdown and release.[5] Chlorite $(Mg,Fe,Al,Mn)_6[(Al,Si)_4O_{10}](OH)_8$ is a 2:1 phyllosilicate which bears close structural and chemical similarities to montmorillonite. In addition, as a breakdown product of biotite mica, it is ubiquitous in the rock mass of altered granitic rocks and mineralized fractures,[6] as well as altered igneous rocks in general. It will also be present in mature iron-bearing mudstones and low-grade metamorphic terraines. Thus, a radiation damage investigation of chlorite is both highly relevant to far-field performance in many candidate rock types

Received: December 17, 2018
Revised: February 25, 2019
Accepted: February 28, 2019
Published: February 28, 2019

DOI: 10.1021/acsearthspacechem.8b00205
ACS Earth Space Chem. 2019, 3, 652−662

and can also act as a proxy for more challenging investigations of other 2:1 clays, such as the engineered bentonite barrier and its constituent mineral phases. Here, controlled α-particle irradiation of a suite of pristine, macrocrystalline, and microcrystalline chlorite samples and subsequent analysis by microfocus techniques has revealed, in previously unrecorded detail, radiation damage manifestations in these 2:1 phyllosilicates. The purity and morphology of these model phases have permitted powerful X-ray analysis techniques, necessary for a mechanistic understanding of light-ion damage accumulation. Based on these novel data, hypotheses regarding the durability of barrier materials under high fluence irradiation can be drawn. Indeed, the findings of this study will have important parallels for damage-induced structural changes across all types of layered materials.

Chlorite group minerals consist of an octahedral sheet of Fe and Mg cations "sandwiched" between sheets of silicon and aluminum-rich, tetrahedrally coordinated 6-membered rings ("TOT" layers); the apexes of the individual tetrahedra point inward toward the octahedral sheet. Rather than a single-cation interlayer between the TOT layers (e.g., biotite mica), chlorites contain a brucite-like interlayer, representative of the types of hydrated interlayers found in smectite, nontronite, etc. This brucite-like layer comprises two sheets of OH^- groups, between which exists another octahedral site, typically filled with Mg or Fe. Hydrogen bonds hold the TOT layers and "brucite-like" interlayers together; a slight lateral offset in stacking results in monoclinic crystal symmetry (see Figure 1).

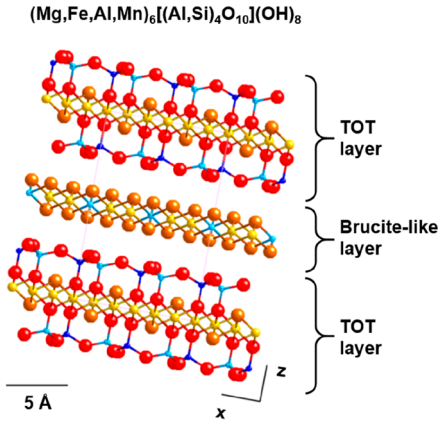

Figure 1. Generalized, schematic crystal structure of chlorite. Octahedrally coordinated metal-rich sheets are bound by tetrahedrally coordinated sheets containing Si and Al. These "TOT" layers are separated by a "brucite-like" sheet, comprising octahedrally coordinated metals and OH^- groups. The representative view is along the (001) plane. [Legend: Si = blue, Al = light blue, O = red, Mg/Fe = yellow; OH^- = orange.] Image generated by CrystalMaker V9.2.7,[7] using a model structure[8] adapted from the Inorganic Crystal Structure Database.[9]

2. METHODS

2.1. Sample Preparation. Two examples of chlorite group minerals were prepared for α-particle radiation damage analysis, differing in chemistry and crystal morphology. Sample type-1 is a large pseudohexagonal (asymmetric) single crystal, from the Val di Susa, in Piedmont, Italy. Electron probe microanalysis (EPMA) (see Table 1, presented later in this work) confirms that the sample can be classified as an impure clinochlore (3.32 ± 0.01 wt % Fe present), with Fe/(Fe + Mg) = 0.07. Samples were prepared as centimeter-scale single crystals, easily separated along the cleavage planes by exfoliation, ∼30 μm thick. In contrast, sample type-2 is a polycrystalline aggregate (locality unknown) and is characteristic of chloritic alteration formed as a product of crustal circulation of hydrous fluids. Chemically, the sample lies along the clinochlore/chamosite solid solution series (21.77 ± 0.01 wt % Fe present) with Fe/(Fe + Mg) = 0.57. The dense mass of fine flakes forms a typically chloritic or "felt-like" texture. Samples were prepared as ∼30 μm wafers from centimeter-scale masses of the polycrystalline chloritic aggregate, with crystallite sizes ranging from 10 to 200 μm. As such, the two contrasting samples allowed a comparison of the molecular scale responses to α-particle irradiation in high and low Fe-bearing chlorite, and larger-scale damage mechanisms manifested in both single-crystal and microcrystalline material. Macrocrystalline samples (type-1) were all irradiated with the incident ion beam perpendicular to the basal plane, such that α-particles would travel "across" the TOT sheets (Figure 1). In contrast, sample type-2 presented multiple orientations to the ion beam in a single "thin" section.

2.2. Ion Irradiation and Damage Quantification. Samples were irradiated under vacuum with a focused 5 MeV $^4He^{2+}$ ion beam, using the Dalton Cumbrian Facility's 5 MV tandem pelletron via an established method.[10−12] The beam was focused into a pseudo-Gaussian profile, such that the center of the beam delivered a much higher dose than the perimeter. In this way, a single sample was able to accumulate a range of doses over a circular beam spot (area = 1 cm^2) suitable for synchrotron microfocus analysis. The beam current was kept consistent at 200 nA across all irradiations to minimize heat loading; a thermocouple mounted to the back of each sample displayed a peak temperature of 87 °C across the 3−5 h irradiations.

The conventional model of α-particle linear energy transfer in a solid was assumed for all irradiations. That is, structural or "knock-on" interactions are maximized at the end of an α-particle's projected range, following a region of steadily increasing energy loss as the ion interacts with the surrounding electric fields, kinetically ejects electrons from target ions as it passes (losing its own kinetic energy in the process), and accepts electrons to render it a neutral atom.[12] In context, a 5 MeV $^4He^{2+}$ particle entering a chlorite-type phase will exhibit a track length of ∼20 μm, with maximum "knock-on" displacements occurring within the final ∼6 μm (the region of maximum structural displacements has a fwhm of ∼2 μm). Such assumptions have been drawn from the modeling software, SRIM,[13] and are based on the density and chemical constituents of a model chlorite mineral.

Subsamples of both sample types were irradiated under two separate dose regimes (Table 1). The "displacements per atom" (DPA) value (the number of times a single atom is relocated in the structure due to the "knock-on" interactions of the incident α-particles) was calculated by averaging the displacements per ion per unit depth (calculated using SRIM), multiplied by the ion fluence and averaging across the atomic density of the sample.[14] The "DPA" value is dependent on the integration area over the beam profile (pseudo-Gaussian). The values presented here are calculated as an average over the α-particle's full 20 μm penetration depth; however, >99% of the structural damage is incurred in the final ∼10% of the ion's track, thus, these values should only be treated as a guide to

DOI: 10.1021/acsearthspacechem.8b00205
ACS Earth Space Chem. 2019, 3, 652−662

Table 1. Sample Details and Administered Radiation Doses

No.	formula[a]	fluence[b]	Displacements Per Atom,[c] DPA (r = 6.6 − 0 mm)	(r = 3 − 2 mm)	(r = 2 − 1 mm)	(r = 1 − 0 mm)	(r = 0.65 − 0 mm)
1-A	$(Mg_{4.85}Al_{0.76}Fe^{2+}_{0.34})[(Si_{3.32}Al_{0.68})O_{10}](OH)_8$	8.76×10^{15}	0.04	0.05	0.11	0.35	0.87
1-B	same as above	3.63×10^{15}	0.02	0.02	0.047	0.14	0.36
2-A	$(Fe^{2+}_{2.57}Mg_{1.91}Al_{1.45})[(Si_{2.70}Al_{1.30})O_{10}](OH)_8$	1.24×10^{16}	0.05	0.06	0.13	0.49	1.12
2-B	same as above	3.88×10^{15}	0.02	0.02	0.05	0.15	0.38

[a]Chemical formulae are recalculated from EPMA data and are accurate to ±0.01 formula units. [b]"Fluence" denotes the total number of $^4He^{2+}$ ions delivered to the sample by the ion beam (beam footprint radius = 6.6 mm). [c]"DPA values show integrated displacements per atom (DPA) values across the total beam footprint and sections of the central 3 mm of the Gaussian ion beam spot for each sample. r denotes the integration range (distances are given as the radius from the centre of the ion beam in mm (expressed in micrometers for microfocus data)) and are representative of the XRD traverses shown in Figures 3 and 4, which are shown later in this paper. DPA calculations are based on SRIM modeling[13] and are averaged across the full penetration depth of the incident ion (20 μm).

relative dose accumulation across the samples in this study. Total ion fluence (a more useful comparator between studies) is also presented in Table 1.

Both sample types displayed a subtle optical response to irradiation. Sample 1, originally green on a fresh surface, darkened to black toward the center of the exposed region. In contrast, sample 2, originally translucent and pale blue/green in color, displayed a faint brown tint after irradiation and the ion beam footprint was optically discernible from the unirradiated region. Table 1 details the comparative doses experienced by each of the four samples studied.

2.3. Electron Probe Microanalysis. Major element analysis of the samples prior to irradiation was undertaken by WD spectrometry using the CAMECA SX-100 electron microprobe at the University of Manchester. Operating conditions and standards are detailed in a prior study.[15] Recalculated formulas (Table 1) are the average over 25 sampling points.

2.4. Synchrotron Microfocus X-ray Diffraction (μXRD) and X-ray Absorption Spectroscopy (μXAS) Measurements. Analysis of radiation damage using a combination of μXRD and Fe *K*-edge μXAS was performed on beamline I18 at Diamond Light Source (double-crystal monochromator). The X-ray beam spot size was focused to a diameter of ∼2 μm in the vertical plane (∼3 μm in the horizontal) and both XRD and XAS data were collected as "traverses" through regions of increasing radiation dose, in step sizes ranging from 30 μm to 100 μm. Transmission diffraction patterns were collected at 12 keV, using the beamline's Photonic Science XDI-VHR 125 CCD, calibrated using either a LaB_6 or Si powder standard. Reflections were indexed using the JEMS software.[16] All patterns were background-subtracted and reduced using a combination of the Nika Plugin for Igor Pro[17] and the DAWN Science suite, Diamond Light Source's in-house data analysis software.[18,19]

Fe *K*-edge X-ray absorption near-edge structure (XANES) data were collected to yield information on radiation-induced Fe speciation changes; complementary extended X-ray absorption fine structure (EXAFS) data were collected to assess changes in local order around the absorbing (Fe) atom. XAS data were collected in fluorescence mode using the beamline's Vortex ME4 SDD, with a maximum energy step of 0.1 eV across the absorption edge. The penetration depth of the X-rays at the Fe *K*-edge is ∼25 μm given the chemistry and density of the samples, thus maximizing the signal from the region of maximum structural damage. XAS data background subtraction, normalization, and fitting was performed using the Demeter suite.[20] Beamline energy was calibrated using an Fe foil with a first derivative maximum of 7112 eV. Reference spectra (FeO, Fe_2O_3) were taken from the XAFS Spectra Library.[21]

2.5. Fourier Transform Infrared (FTIR) Spectroscopy. Fourier transform infrared (FTIR) analysis was performed using the University of Manchester's Spotlight 400 TM spectrometer in attenuated total reflectance (ATR) mode. The irradiated "thin" sections of chlorite were placed flat against the ATR crystal (irradiated side down) and scanned in high resolution across the characteristic absorption window for the OH^- stretching region (3800−3300 cm^{-1}). Spectra were reduced and normalized in the specialist FT-IR analysis software OMNIC (Thermo Electron Corporation 2004).

3. RESULTS

3.1. Microfocus X-ray Diffraction. Sample type-1 is the macrocrystalline sample; therefore, reflections appeared as discrete "spots" in the CCD images. Diffraction patterns were collected at 30 μm intervals across both an unirradiated control sample and irradiated sample type 1-A (Figure 2).

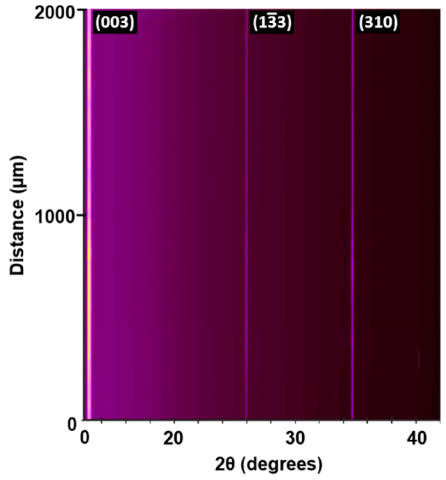

Figure 2. Composite μXRD map across an unirradiated, control sample of chlorite type-1. The consistency (both in position and intensity) of each of the three reflections (003), (1$\bar{3}$3), and (310) denotes a single crystal that is structurally homogeneous over >2 mm. The image is built from 67 diffraction patterns collected at 30 μm intervals along a 2000 μm traverse.

DOI: 10.1021/acsearthspacechem.8b00205
ACS Earth Space Chem. 2019, 3, 652−662

Three reflections are visible in Figure 2, collected from the control sample. At the lowest detectable angle, the basal plane parallel (003) reflection was observed at d = 4.74 Å, as well as two high-angle basal plane subperpendicular reflections ($1\bar{3}3$) (d = 2.26 Å) and (310) (d = 1.72 Å). Each peak remains consistent in intensity and diffraction angle across the traverse, indicative of a structurally homogeneous phase.

Figure 3 shows a 3 mm traverse across the irradiated sample type 1-A, into the region of highest radiation dose (the center of the ion beam footprint). The same three reflections observed in the control sample are also consistently present in sample 1-A. However, several additional reflections appear in the μXRD map; two clusters of new reflections between 23° and 24° 2θ and 38°−42° 2θ are sporadically visible along the traverse. It is difficult to accurately assign these minor reflections due to their diffuse nature and often broad, poorly resolved peaks. An inconsistent peak at 22.5° 2θ (2.69 Å) matches the expected position for the chlorite (−132) reflection; interestingly, this lattice dimension should not be visible in the given analysis orientation. The appearance of such minor peaks are evidence for the distortion of regions of the lattice on a micrometer scale. Higher angle reflections cannot confidently be assigned due to the competing interferences of lattice parameter distortions and the emergence of "forbidden" reflections; however, their intermittent presence is clear evidence for the development of microscale mosaicism within this single-crystal sample.

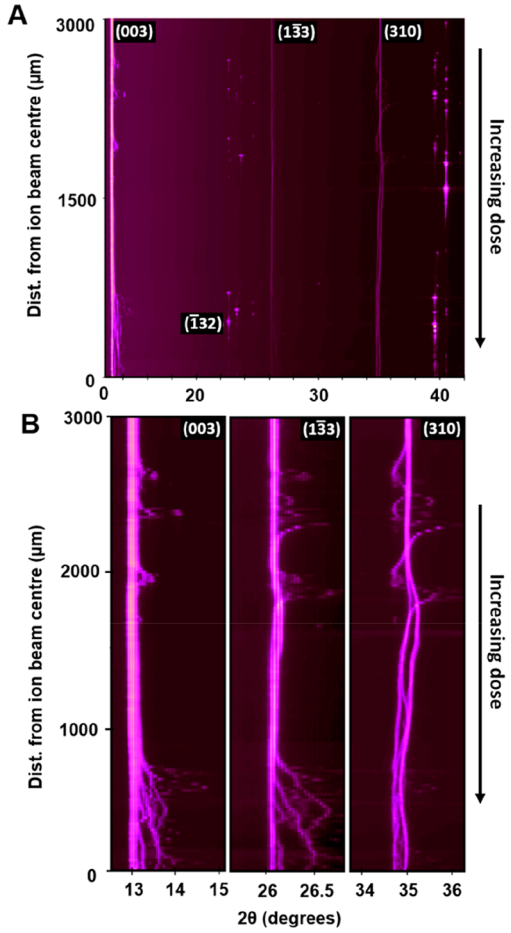

Figure 3. (A) Composite μXRD map across the highest dose region of sample 1-A (3 mm radius from the ion beam center; see Table 1). The three peaks observed in the unirradiated material (Figure 2) show extensive aberrations, shown in the magnified maps (see panel (B)). The image is built from 100 diffraction patterns collected at 30 μm intervals along a 3000 μm traverse.

The three most pervasive reflections, as observed in the control specimen, also reveal drastic changes in lattice parameter consistency following irradiation. The basal plane parallel (003) reflection remains present across the traverse and matches the consistency of the control sample until ∼3000 μm from the maximum region of radiation damage. Observable intermittently over ∼2500 μm and manifesting significantly at ∼650 μm from the peak of ion dose (∼0.87 DPA), the reflection splits into many peaks of higher 2θ value, representing multiple, metastable contracted lattice domains. The μXRD map reveals the complexity of this peak splitting, as some satellite peaks themselves split further, suggesting an aggregation of damaged domains with variably collapsed interlayers. Rather than simply broadening with increased defect density, as commonly reported for radiation damaged materials, many of the bifurcating peaks can be traced uninterrupted across several micrometers, suggesting that the response to ion irradiation is the production of multiple microdomains with a degree of crystallinity and interconnectivity. Despite extensive peak splitting, the "main" reflection remains constant across the entire traverse, suggesting that broad regions of the original structure remain, alongside heavily altered domains. It is likely that a proportion of this signal originates either as a contribution from the low structural interaction region of the $^4He^{2+}$ ion beam (see section 2.2), as it is difficult to fully isolate the horizon of maximal structural damage (which likely deepens with increasing dose). Reflection ($1\bar{3}3$), a plane of octahedral cations subperpendicular to the TOT sheets (Figure 1), displays almost identical 2θ shifts as that observed for the (003) peak, with the exception of a more pronounced shift of the "main" reflection to higher 2θ angles at ∼2000 μm from the ion beam center, manifested as a "kink" in the diffraction map trace at ∼1600 μm.

The high angle (310) reflection represents a plane parallel to the z-axis, thus giving an insight into the response of the lattice perpendicular to the TOT sheets. At ∼ 2000 μm from the point of maximum of ion beam fluence, the lattice disruptions are manifest as a "split" peak as the received dose increases. At ∼ 1600 μm from the peak of ion dose (0.11 DPA), the (310) peak bifurcates into two peaks of equal intensity (d = 1.71 and d = 1.73) and these persist into the region of maximum dose, suggesting two discrete "damaged" domains existing in parallel. Both metastable reflections show distinct sinusoidal movements on a millimeter scale, suggesting lattice "bulging" and "contraction". Interestingly, there is a distinct spatial correlation across all three peaks at points of abrupt lattice change, revealing the doses at which defect loading becomes so high that the consequent lattice distortions are evident across all reflections.

The polycrystalline type-2 chlorite (2-A) experienced the highest dose of all samples irradiated. Because of the microcrystalline nature of the sample prior to irradiation, both the unirradiated and irradiated diffraction patterns appeared as rings in the CCD images, and patterns were collected at much larger steps; thus, the data is displayed as reduced 1D patterns for clarity. Figure 4 shows the 1D patterns for chlorite 2-A across specific indexed reflections. As with sample 1-A, the (003) peak (d = 4.62 Å) (Figure 4A) denotes

DOI: 10.1021/acsearthspacechem.8b00205
ACS Earth Space Chem. 2019, 3, 652−662

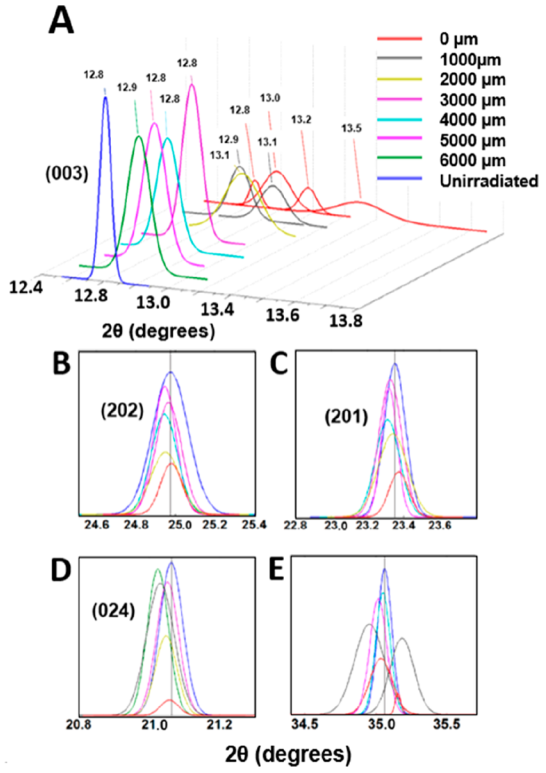

Figure 4. Microfocus diffraction patterns collected across the irradiated polycrystalline chlorite type 2-A. Each pattern denotes a 1000 μm step along the traverse, given as a distance from the center of the ion beam spot (see Table 2). Panels (A)−(E) show isolated reflections. Distances stated are ±100 μm.

a reflection parallel to the basal or cleavage plane, an effective measure of the changes in interlayer spacing. Across the traverse, the (003) reflection shifts to higher 2θ angles with increasing dose, the decrease in d-spacing demonstrating the collapse of the phyllosilicate layers with increasing radiation damage. At the areas receiving the highest dose and attendant radiation damage (1.12 DPA across the last 650 μm of the traverse), the (003) reflection has split into four discrete, yet broad, peaks, showing that the structure breaks down into discrete crystallites with varying interlayer spacing. The diffuse peak centered at 13.49° 2θ (d = 4.38 Å) suggests a collapse of as much as 0.24 Å from the undamaged lattice spacing in some regions of the damaged structure. This shift is comparably smaller than the maximum observed for the macrocrystalline sample (1-A), which contracted by as much as 0.5 Å, in comparison with the unirradiated pattern (within 1000 μm of the peak of ion dose). However, the average degree of basal plane collapse is comparable across both samples, and spatial variations were expected to be this extensive.

Reflections (202) (d = 2.37 Å) and (201) (d = 2.55 Å) (Figures 4B and 4C) denote atomic planes subperpendicular to the basal plane along the x-axis. Using the unirradiated standard pattern as a reference point (control peak positions shown by the vertical line on each 2D pattern in Figure 4), both peaks show a shift to lower 2θ angles of varying magnitude across the initial 4000 μm of the traverse, at a region of lower dose than the observed splitting of peak (003). However, over the region of the mineral subjected to the maximum dose, both reflections show a very slight shift to higher 2θ values than the reference reflections (central 1000 μm). It is evident again that the structure expands and contracts variably in the x-plane; reflecting increased damage and defect loading until the highest doses, whereupon peaks are significantly broadened and less intense. Reflection (024) (Figure 4D) is oriented subperpendicular to reflections (201) and (202), such that information on lattice dimensions in the y-axis is revealed. A similar trend of lattice expansion is also revealed in this plane with increasing damage. Peak splitting is also evident, as displayed by the unindexed reflection (at ∼35.052° 2θ) in Figure 4E. Similar to that observed for the monocrystalline sample, both patterns at 2000 and 1000 μm from the ion beam center show the original single peak splitting into two discrete peaks at higher and lower 2θ angles. Peak broadening is pervasive across the traverse of the polycrystalline sample, highest at the peak of ion dose, as point defect densities reduce the consistency of the diffracting atomic planes and broaden the range over which Bragg reflections are permitted.

3.2. Microfocus X-ray Absorption Spectroscopy. Fe K-edge XANES and EXAFS data were collected from both samples at spot points along the XRD traverses detailed above. Figure 5 shows representative Fe K-edge XANES data across samples 1-A and 2-A (maximum dose) and 2-B (low dose), as well as the unirradiated standard, presented alongside reference spectra (FeO and Fe_2O_3).

Figure 5A−C shows a XANES traverse (500 μm steps) across sample type 1-A. Subtle peak damping is observed in the spectra with increasing radiation dose (decreasing distance from the ion beam center). A slight decrease in the edge-step and a broadening in the absorption edge toward lower energies (arrow 1, Figure 5A) may indicate Fe reduction in the sample at these doses, evidenced also by the slight shift of the zero intersection of the white line in the first derivative plot (arrow 2, Figure 5C).

Similar data were collected across samples 2-A and 2-B. Spectra collected from the low-dose samples, (Figure 5D−F; Sample 2-B), share commonalities with those from sample 1-A (Figure 5A−C). Chiefly, a minor loss in oscillation amplitude beyond the edge, as well as a slight reduction in the edge step, which is consistent with increased defect densities resulting in local disorder.[12] Most notably, a "shoulder" appears on the low energy side of the edge, at ∼7122 eV (arrow 3, Figure 5D). While not a definitive shift of the absorption edge (first derivatives of the spectra do not show a pronounced edge-shift), increased spectral features at energies below the edge may also suggest a lowering of the average electron binding energy for iron, which occurs with a decrease in the oxidation state of Fe. Indeed, these spectra bear similarities with the FeO reference spectrum.

In comparison, in the highest dose region of 2-A (Figure 5D), a severe damping of the absorption edge due to radiation damage is evident. The white line region broadens toward higher energies (evident also in the first derivative plots, Figure 5F) and the spectral features within the region above the edge are "smeared" as radiation damage is manifest by a marked loss of short-range order, consistent with the XRD data (arrow 4, Figure 5D). Severe damping such as this is often associated with self-absorption effects, however no significant changes in sample-thickness, Fe concentration or analysis parameters can account for this over such a small area, therefore the effect is wholly a product of radiation damage.

As with samples 1-A and 1-B, confident interpretation of a change in Fe oxidation state across sample 2-A is challenging.

DOI: 10.1021/acsearthspacechem.8b00205
ACS Earth Space Chem. 2019, 3, 652−662

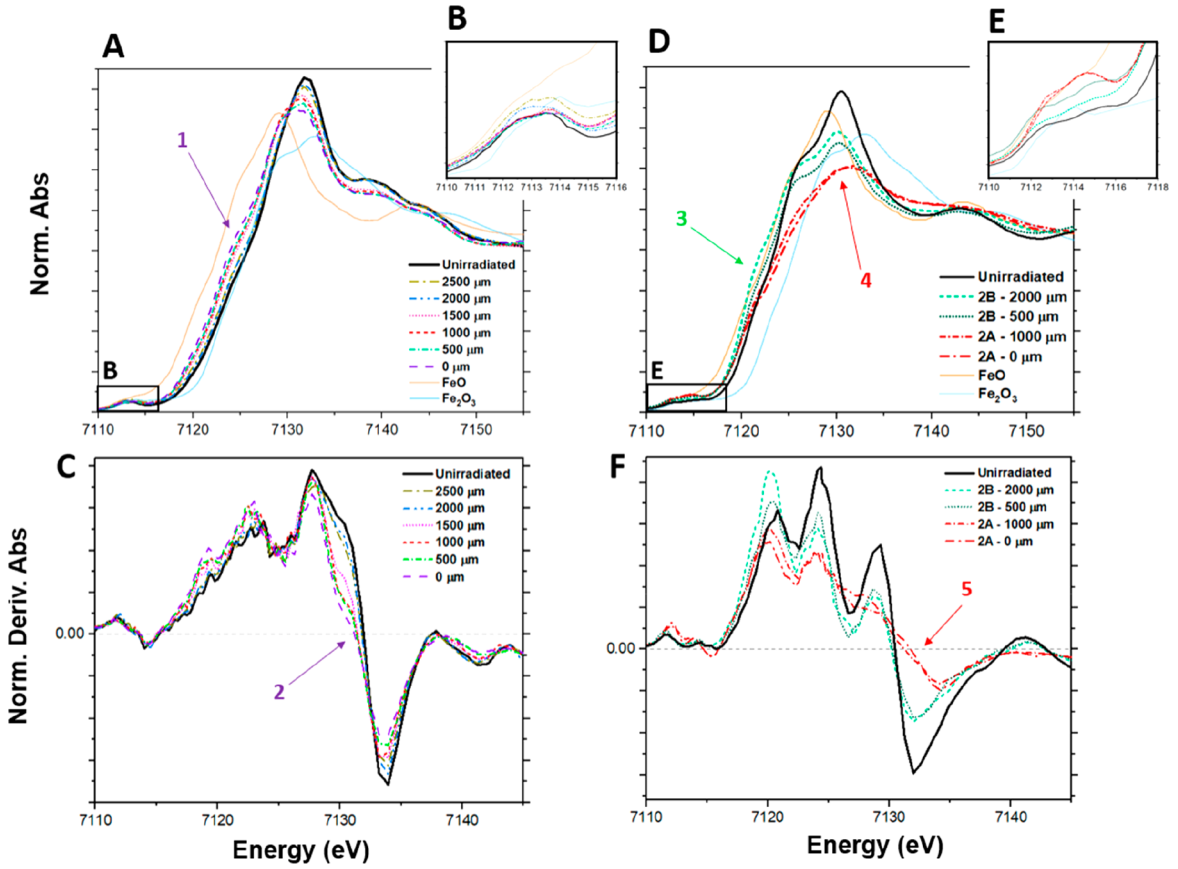

Figure 5. Microfocus Fe *K*-edge XANES spectra collected across the irradiated chlorite samples. (A) Representative Fe *K*-edge XANES spectra across an unirradiated section of chlorite and six points at sequentially increasing doses across chlorite 1-A, collected at 500 μm intervals from 2500 to 0 μm (distance from ion beam centre), see Figure 3. Reference spectra, from FeO and Fe_2O_3 are included for comparison. (B) Insets show the pre-edge region of spectra, expanded for clarity. (C) Corresponding first derivatives of the XANES data in panels (A). (D) Representative Fe *K*-edge XANES spectra across an unirradiated section of chlorite type-2 and two points at sequentially increasing doses across irradiated chlorite 2-A, as well as two points across irradiated chlorite 2-B. (E) Insets show the pre-edge region of spectra, expanded for clarity. (F) Corresponding first derivatives of the XANES data in panel (D). Distances stated are ±100 μm.

The "shoulder" on the lower energy side of the edge is broadly lost, as is the peak at ~7125 eV, in contrast to the spectra from sample 1-A. There is a slight indication from the first derivatives (arrow 5, Figure 5F) of an oxidative shift of the white line. However, it is difficult to isolate this from line broadening due to severe defect accumulation. Qualitative assessment of the pre-edge features shows a pronounced peak appearing at 7115 eV (Figure 5E), which may also be linked to Fe oxidation at these doses. Pre-edges denote bound state transitions in metals; generally, the intensity weighted average position of the pre-edge components denotes the oxidation state of the iron; a shift toward higher energy of this "centroid" denotes a more oxidized proportion of the Fe.[22] Note that sample 2-B has only received ~60% of the dose of sample 2-A. Radiation damage clearly has a significant effect upon short-range atomic order within the chlorite, qualitatively demonstrated in the XANES signals here by aberrations in the pre-edge and post-edge modulations.

Figure 6 displays the EXAFS data (and fits) for each of the corresponding XANES plots displayed in Figure 5. Despite low data resolution, three independently varying paths could be fitted across each dataset. Paths were not added if they did not contribute a 5% improvement in the overall fit. A shell of octahedrally coordinated oxygens; a second shell of Fe (representing neighboring metal cation in the octahedral sheet) and a third shell of silicon scatterers (from the tetrahedrally coordinated atoms in the overlying and underlying sheets of the TOT). Closely neighboring second and third shells were manifest as a single broad peak in the Fourier transform, particularly in the damaged structures. Across all fits, interatomic distance and Debye–Waller factors (disorder parameters) were allowed to vary independently. Shell occupancies (coordination numbers) were fixed across all fits, because of the models being unable to confidently resolve realistic values in radiation-damaged samples when these parameters were floated. Amplitude reduction factors were fixed for fitting but altered between fits in some instances to improve the *r*-factor, compensating for fixed coordination numbers in the damaged structures' models and the marked damping discussed previously. Table 2 shows the EXAFS fit results for all of the spectra shown in Figure 6.

Sample type 2-B, the lowest dose sample of those studied by XAS, shows a general increase in the disorder factor (the Debye–Waller factor, σ^2) in the second and third shells with increasing dose (decreasing distance from beam center), compared with the unirradiated standard. Despite the small "shoulder" appearing on the low energy side of the absorption edge (possibly indicative of Fe reduction), Fe–O bond lengths remain consistent within error of the standard, although 2B-

DOI: 10.1021/acsearthspacechem.8b00205
ACS Earth Space Chem. 2019, 3, 652–662

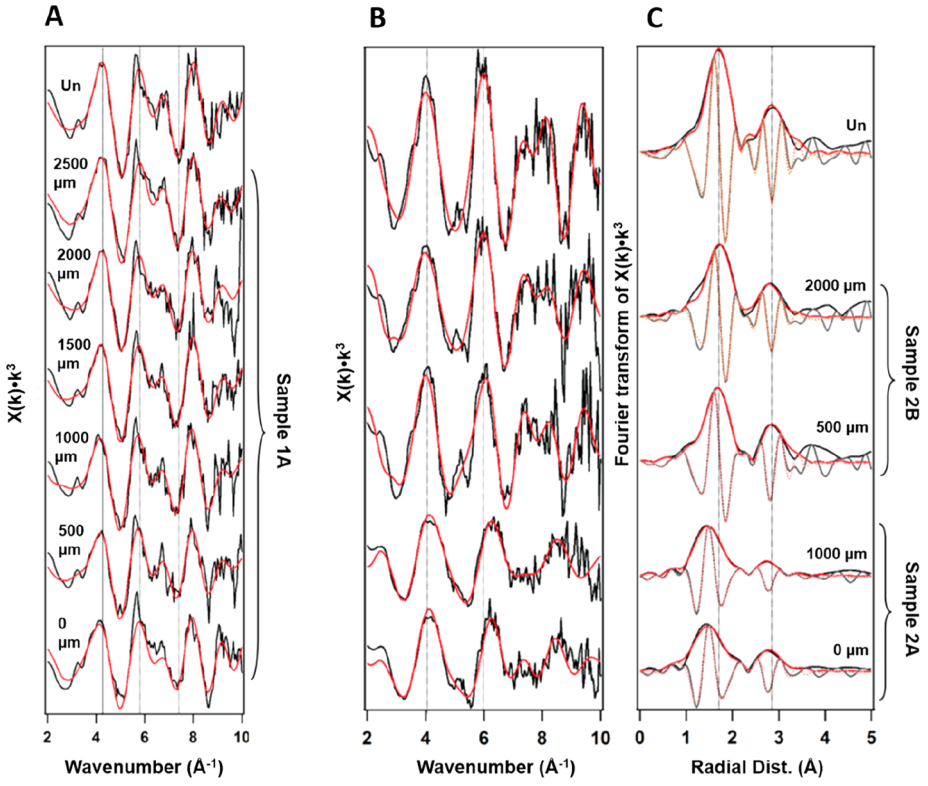

Figure 6. Microfocus EXAFS fit results from corresponding XANES shown in Figure 5. (A) *k*-space data (black) and fits (red) across sample 1-A, as well as an unirradiated sample (Un). Spectra represent a 2500 μm traverse in 500 μm steps into the region of maximum ion dose. (B) *k*-space data (black) and fits (red) across selected points from samples 2-A and 2-B, as well as an unirradiated sample (Un). (C) Non-phase-corrected Fourier transform of data displayed in panel (B), showing distances from the center of the ion beam (region of highest radiation dose). Spectra have been offset vertically for clarity and reference lines from major oscillations/peaks in the unirradiated sample have been drawn. Distances stated are ±100 μm.

1000 μm could not confidently be fit with a Fe−O coordination number (CN) of >4.0.

Spectra collected from the highest dose sample (2-A) display the highest deviation in the modeled fits from the unirradiated standard. Data are best fit by decreasing Fe−O coordination numbers (6.00 to 3.50−parameters fixed) as well as the Fe−M[1] coordination numbers (6.00 to 4.00−parameters fixed). Fe−O interatomic distances are significantly shortened, compared to the unirradiated standard (2.12 ± 0.01 to 1.99 ± 0.01) and second and third shell bond lengths also shorten to 3.12 ± 0.02 and 3.25 ± 0.01, respectively for 2-A-1000 μm. Fe−M[1] Debye−Waller factors are also at their highest across the most damaged sample (up to 0.027 ± 0.001), indicative of a wide variation in the mean half path length for these shells. Qualitatively speaking, a marked loss in oscillation amplitude is observable between the unirradiated signals and the areas at the peak of damage (Figure 6); this also manifests as a damping and broadening of the second peak in the Fourier transform.

In contrast, a slight increase in first shell Fe−O distances is apparent across sample type 1-A (from 2.04 ± 0.1 to a maximum of 2.07 ± 0.1). Second-shell coordination remains constant (i.e., fits were not improved by varying the shell occupancy), while a small decrease in shell occupancy is notable in the third (Fe−Si) shell. A consistent lengthening of the second and third shell spacing is apparent; in some instances, the modeled bond length of the Fe−Si shell increases by 0.35 Å. These values should be treated with caution, as a very high DW factor (>0.03) implies extreme disorder, or that the fixed CN may be an overestimate. Errors on these DW factors were also very high; therefore, since fits were statistically improved with the addition of these shells, the paths were included in all models for completeness.

3.3. Fourier Transform Infrared Spectroscopy. Figure 7 shows the absorption across the hydroxyl stretching region of the chlorite 1-A Infra-Red (IR) spectrum. Experimental geometry dictated that the interaction region of the IR beam (~2−5 μm depth) did not reach the region of maximum structural damage within the crystal (~18−20 μm); despite this the spectra display interesting changes. Two distinct bands are evident in the unirradiated standard, the most intense at 3599 cm^{-1} and a second at 3470 cm^{-1}. Prior work[23] has noted that hydroxyl groups absorbing within this narrow region are involved in hydrogen bonds, belonging to the interlayer set of hydroxyl groups with the bonds perpendicular to the basal plane; the higher and lower frequency peaks are bonded to (SiSi)O and (SiAl)O in the overlying and underlying tetrahedral sheets, respectively. Upon irradiation, the doublet broadens, and both peaks shift to lower wavenumbers. The same study[20] ascribes such a shift to an increase in both tetrahedral Al and octahedral Fe in chlorites of varying compositions, although this is unlikely to be the case in the irradiated sample unless such a response derives from an increase in interstitial defects in the sheets. A shift to lower frequencies of hydroxyl group bands is more generally indicative of an increase in the strength of hydrogen bonding,[24] weakening the oxygen−proton bond.[25] While this seems counterintuitive in a radiation-damaged sample, this may be

DOI: 10.1021/acsearthspacechem.8b00205
ACS Earth Space Chem. 2019, 3, 652−662

Table 2. EXAFS Fit Results for All Spectra Shown in Figure 6[a]

spectrum	path[b]	CN[c]	R^d (Å)	Debye–Waller factor, σ^2	amplitude reduction factor, S_0^2	goodness of fit, r
			Sample Type 1			
unirradiated	Fe–O	6.0*	2.04 ± 0.01	0.008 ± 0.002	0.75*	0.006
	Fe–M^1	6.0*	3.02 ± 0.02	0.006 ± 0.002		
	Fe–Si	4.0*	3.09 ± 0.02	0.001 ± 0.001		
1A, 2500 μm	Fe–O	6.0*	2.04 ± 0.01	0.009 ± 0.001	0.80*	0.010
	Fe–M^1	6.0*	3.12 ± 0.02	0.005 ± 0.005		
	Fe–Si	4.0*	3.45 ± 0.02	0.025 ± 0.011		
1A, 2000 μm	Fe–O	6.0*	2.07 ± 0.01	0.010 ± 0.001	0.75*	0.007
	Fe–M^1	6.0*	3.13 ± 0.01	0.005 ± 0.002		
	Fe–Si	4.0*	3.14 ± 0.08	0.057 ± 0.010		
1A, 1500 μm	Fe–O	6.0*	2.06 ± 0.01	0.008 ± 0.001	0.70*	0.010
	Fe–M^1	6.0*	3.11 ± 0.02	0.003 ± 0.004		
	Fe–Si	4.0*	3.32 ± 0.01	0.050*		
1A, 1000 μm	Fe–O	6.0*	2.07 ± 0.01	0.008 ± 0.002	0.70*	0.010
	Fe–M^1	6.0*	3.12 ± 0.01	0.003 ± 0.004		
	Fe– Si	4.0*	3.33 ± 0.01	0.050*		
1A, 500 μm	Fe–O	6.0*	2.06 ± 0.01	0.010 ± 0.001	0.70*	0.011
	Fe–M^1	6.0*	3.12 ± 0.01	0.005 ± 0.002		
	Fe–Si	2.0*	3.52 ± 0.01	0.033 ± 0.018		
1A, 0 μm	Fe–O	6.0*	2.06 ± 0.01	0.009 ± 0.001	0.70*	0.006
	Fe–M^1	6.0*	3.13 ± 0.01	0.004 ± 0.002		
	Fe–Si	3.0*	3.15 ± 0.01	0.046 ± 0.026		
			Sample Type 2			
unirradiated	Fe–O	6.0*	2.12 ± 0.01	0.008 ± 0.002	0.70*	0.016
	Fe–M^1	6.0*	3.12 ± 0.02	0.012 ± 0.004		
	Fe–Si	4.0*	3.35 ± 0.02	0.005 ± 0.003		
2B, 2000 μm	Fe–O	4.0*	2.13 ± 0.02	0.007 ± 0.001	0.70*	0.012
	Fe–M^1	6.0*	3.10 ± 0.02	0.014 ± 0.003		
	Fe–Si	4.0*	3.34 ± 0.02	0.008 ± 0.005		
2B, 500 μm	Fe–O	6.0*	2.12 ± 0.01	0.014 ± 0.001	0.75*	0.017
	Fe–M^1	6.0*	3.11 ± 0.02	0.018 ± 0.002		
	Fe–Si	3.0*	3.35 ± 0.03	0.005 ± 0.001		
2A, 1000 μm	Fe–O	3.5*	1.99 ± 0.01	0.012 ± 0.001	0.70*	0.009
	Fe–M^1	4.0*	3.06 ± 0.02	0.027 ± 0.001		
	Fe - Si	4.0*	3.25 ± 0.01	0.013 ± 0.001		
2A, 0 μm	Fe–O	4.0*	2.01 ± 0.01	0.014 ± 0.001	0.70*	0.014
	Fe–M^1	4.0*	3.08 ± 0.02	0.024 ± 0.005		
	Fe–Si	4.0*	3.26 ± 0.01	0.009 ± 0.001		

[a]An asterisk symbol (*) beside a value denotes that the parameter was fixed during the fitting. Distances stated are ±100 μm. [b]M^1 denotes the neighboring octahedral metal cation site, modelled as Fe. Shells were not included unless there was a >5% improvement in the fit. [c]CN denotes coordination number (±1.0), fixed based on the best fit to the data. [d]R denotes interatomic distance. Distances (given in μm) represent distance from beam centre (radiation damage maximum).

a response of the interlayer collapse shortening the (SiSi)O–OH distances. Nevertheless, the interaction depth is likely too shallow to reveal the truly dehydrated region probed by XRD.

4. DISCUSSION

The data allow several assertions to be made regarding the structural and chemical responses of chlorite to α-irradiation at varying doses. Collapse of the interlayer spacing is consistent with previous studies of radiation damaged phyllosilicates.[12] At the point of maximum dose, a contraction of up to 0.5 Å of the basal (003) plane was observed in both chlorite samples. This collapse is explained by the partial destruction of the "brucite-like" layer, which is the weak component of the chlorite structure and likely more susceptible to breakdown than the

DOI: 10.1021/acsearthspacechem.8b00205
ACS Earth Space Chem. 2019, 3, 652–662

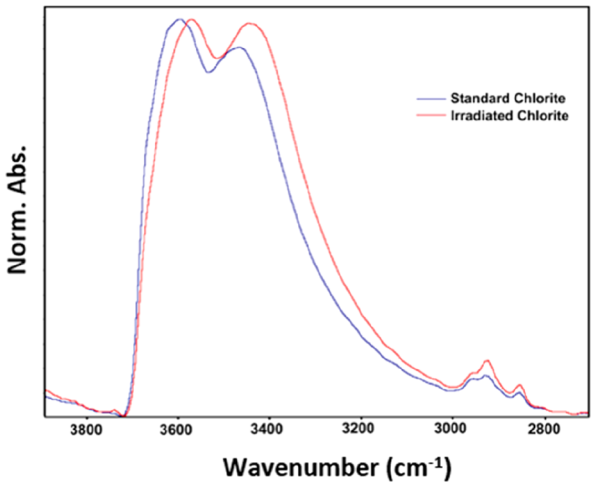

Figure 7. FTIR spectrum centered across the OH stretching region of both the standard, unirradiated sample and irradiated sample 1-A (8.76×10^{15} ions/cm^2). Note the shift of the stretching frequency to lower wavenumbers in the irradiated sample.

cation-rich (K^+) interlayers of more refractory phyllosilicates, such as mica. Indeed, a contraction of this magnitude is consistent with complete interlayer dehydration, as observed in heat-treated chlorites,[26] although it is likely that complete interlayer dehydration is maximized only at a specific depth in the crystal, coincident with the region of maximum knock-on damage along an α-particle's trajectory (~18−20 μm). The damaged crystal is likely held together by a patchwork of partially hydrated domains, evidenced by the "branching" of basal plane parallel peaks shown in Figure 3, revealing a multitude of semistable interlayer distances over ~500 μm.

Variable degrees of lattice expansion and contraction have been demonstrated in planes subnormal to the [00l] direction, with the structure breaking down into randomly oriented crystallites with highly irregular lattice dimensions. Such "mosaicism" has also been observed in our previous investigations and has been attributed to increasing point defect densities causing variable strain and heterogeneous lattice collapse. This is likely combined with the propensity for "bubble" formation in the structure, induced by helium gas build up at, or near, the surface.

Large, amorphous regions are not observed at the investigated doses. Instead, it appears that discrete new crystallites, a variation of dehydrated chlorite, are created. The major structural changes seen in the (003) and ($1\bar{3}3$) planes in the diffraction maps (Figure 3) are coincident and reveal development of discrete new, "metastable" structures derived from the original chlorite lattice. The bifurcation of the (310) peak (Figure 3) indicates a metastable phase comprising two discrete unit-cell parameters (or unique structures) at d = 1.71 and d = 1.73 that persist at high doses. The emergence of sporadic new reflections is attributable to the reorientation of discrete domains of the structure, revealing new lattice planes that satisfy Bragg diffraction in the orientation of the X-ray beam. These reflections cannot be confidently assigned to an existing mineral structure or alteration phase and can only reasonably be interpreted as a dehydrated phyllosilicate-like structure. Reflections at ~40° 2θ (Figure 3) reveal regions of the lattice with low d-spacing (<1.5 Å); the emergence of these reflections (and their difficulty to confidently assign to a chlorite mineral structure) may indicate the possible emergence of minor alteration phases resulting from the collapse of the hydrated interlayer; however, confident reflection indexing is a challenge. It is important to note that the entire phyllosilicate group has a large range of 1:1 and 2:1 stable layered structures of varied d-spacing; while no reflections observed here could be confidently attributed to "secondary" breakdown products, metastable phyllosilicate phases within the damaged chlorite structure are a possibility. Despite the large collapse in the chlorite interlayer spacing, any new basal plane reflection angles are still too low to suggest the presence of a 1:1 clay phase formation.

XAS analysis may suggest a trend toward radiation induced Fe reduction at doses $<9 \times 10^{15}$ ions/cm^2, as observed in similar studies.[10] The trend is subtle, because of the high natural Fe^{2+}/Fe^{3+} ratios in the chlorite sample, but suggests a proportion of the structural Fe^{3+} is reduced by ion irradiation. Fe reduction in α-irradiated phyllosilicates has been postulated to occur *via* several methods; primarily (i) the recycling and consequent migration of electrons from surface to depth by the incident α-particles, combined with (ii) the liberation of reducing radical electrons generated by the damage induced dissociation of OH^- groups. The potential for electron donation by O atoms displaced from the structure has also been suggested.[15] Interestingly, the sample accumulating the highest dose in this study (2-A: 1.24×10^{16} ions/cm^2) did not exhibit a proportional increase in reduced Fe. Indeed, the observed broadening of the white line toward *higher* electron binding energies (and thereby possible Fe oxidation) may reflect a manifestation of the *final* processes of lattice breakdown that occur following the commonly observed reduction at lower doses. Under the extreme bombardment of positively charged alpha particles, the OH^- groups are removed, the structure is increasingly destroyed and the pathways for electron migration disrupted. An excess of positive ions continues to penetrate the structure and locally strip electrons from the most oxidizable component; the high concentration of Fe^{2+}. It is likely that, in the instance of extremely high doses, α-particles can penetrate deeper into the structure, as the stopping power of the damaged crystal is reduced. In this instance, the "zone" of electron stripping may also migrate deeper into the mineral and a dose-dependent redox gradient is formed through the damaged crystal.

EXAFS analysis can help to elucidate the changes in local structural disorder surrounding the Fe, but it is difficult to find consistent trends across the fit results in this study. In the highest dose sample (2-A), Fe−O bond lengths are shortened in the irradiated region compared to the standard which is further indicative of an increased proportion of Fe^{3+} at very high doses. In contrast, Fe−O distances in the lower dose (reduced) samples show a slight increase, but it is difficult to confidently assign a trend within the error of the fit. As previously mentioned, this may be due to recognizing changes in chlorites which have high existing Fe^{2+} contents, compared to reducible Fe^{3+}. Variability in Fe−Fe distances (along layers) is consistent with the μXRD data, showing lattice dilation and contraction within sheets; however, the EXAFS fitting cannot confirm the "collapse" observed by XRD, because the local environment probed by EXAFS does not extend across the TOT sheets. Debye−Waller factors and associated errors again increase with dose, suggesting increased disorder across all modeled paths.

DOI: 10.1021/acsearthspacechem.8b00205
ACS Earth Space Chem. 2019, 3, 652−662

5. CONCLUSIONS

The effect of high fluence α-particle bombardment on chlorite minerals is the spectacular breakdown of the original structure and the generation of domains of new layered structure, in a manner similar to that observed in biotite. The difference in the interlayer in these 2:1 phyllosilicates (brucite layer in chlorite, K^+ in biotite) has an effect on the amount of damage caused, with chlorite being more affected by the easily disrupted brucite layer. Since phyllosilicates, including bentonite, have a range of interlayer structures, a range of responses to α-particle damage is expected, although the product is always likely to be a series of highly reactive microdomains of layered structure with variable *d*-spacing. Further work upon the interaction of these damaged structures with safety-case-relevant radionuclides and suitable analogues is a necessary research avenue, particularly because these damaged structures will likely display vastly different uptake behavior. It is likely that these warped structures will display a vast increase in available "edge" sites, coupled with a wide variation in interlayer distance and consequent migration pathways for ions (although, generally, the interlayer collapse may have a negative effect on ion incorporation). Many studies exist encompassing the uptake of radionuclides on pristine phyllosilicate mineral species, detailing both interlayer incorporation[27,28] and frayed edge/surface site binding.[29−33] Many of these also note the reducing capacity of Fe-rich phyllosilicates in the reductive immobilization of redox active radionuclides;[34−36] however, uptake efficiency in these systems has been demonstrated to be negatively impacted by microbially mediated increases in Fe(II).[37] α-particle damage has the potential to affect each of these mechanisms, although it is unclear the extent to which radiation damage will be detrimental to the safety case for a GDF. However, the same fluid pathways in the GDF near-field, and those that enhance chlorite and other clay development in a GDF far-field will be accessed by migrating radionuclide-bearing fluids, thus increasing the importance to the safety case of these minerals, the radiation damage they suffer, and their reactivity. It is likely that, at relatively "low" doses (before complete amorphization of the structure), the immobilization capacity of clay minerals is increased by α irradiation. However, there will presumably be a dose threshold above which mineral dissolution and release of radionuclides is enhanced; this may be coupled with microparticulate or nanoparticulate release from extensively damaged structures with enhanced environmental mobility.

AUTHOR INFORMATION

Corresponding Author

*E-mail: william.bower@helsinki.fi.

ORCID

William R. Bower: 0000-0003-2070-2483

Carolyn I. Pearce: 0000-0003-3098-1615

J. Frederick W. Mosselmans: 0000-0001-6473-2743

Present Addresses

[▽]Idaho National Laboratory, Idaho Falls, ID 83415, USA.

[#]Pacific Northwest National Laboratory, Richland, WA 99352, USA.

[○]Radiochemistry Unit, Department of Chemistry, University of Helsinki, Helsinki 00510, Finland.

Notes

The authors declare no competing financial interest.

ACKNOWLEDGMENTS

The authors are extremely grateful for the high-quality sample sectioning and preparation throughout the project performed by Stephen Stockley (University of Manchester) and the technical expertise and precision fabrication provided by Barry Gale and Lee Paul (University of Manchester). W.R.B. acknowledges NERC for funding under the DTA grant scheme awarded to the University of Manchester (Code No. NE/K500859/1). The authors are also grateful to Diamond Light Source, U.K., for analysis time on Beamline I18 (Beamtime Award Nos. SP9044 and SP9598) and invaluable project assistance. We also acknowledge the support of The University of Manchester's Dalton Cumbrian Facility (DCF), a partner in the National Nuclear User Facility, the EPSRC UK National Ion Beam Centre and the Henry Royce Institute. Spotlight 400 FTIR and Bruker D8 XRD data were collected in the University of Manchester's Williamson Research Centre, and the authors acknowledge John Waters for assistance with XRD data collection.

REFERENCES

(1) Sellin, P.; Leupin, O. X. The use of clay as an engineered barrier in radioactive waste management - a review. *Clays Clay Miner.* **2013**, *61* (6), 477−498.

(2) Lee, S. Y.; Tank, R. W. Role of clays in the disposal of nuclear waste: A review. *Appl. Clay Sci.* **1985**, *1* (1−2), 145−162.

(3) Svensson, D. *The Bentonite Barrier - Swelling Properties, Redox Chemistry and Mineral Evolution*; Lund University, 2015.

(4) Delage, P.; Cui, Y. J.; Tang, A. M. Clays in radioactive waste disposal. *Journal of Rock Mechanics and Geotechnical Engineering* **2010**, *2* (2), 111−123.

(5) UK Nuclear Decommissioning Authority (NDA). *Geological Disposal—Generic Post-Closure Safety Assessment*; Report No. NDA/RWMD/030, 2010.

(6) Morad, S.; Sirat, M.; El-Ghali, M. A. K.; Mansurbeg, H. Chloritization in Proterozoic granite from Äspö Laboratory, south-eastern Sweden: Record of hydrothermal alterations and implications for nuclear waste storage. *Clay Miner.* **2011**, *46* (03), 495.

(7) *CrystalMaker: V9.2.7: A Crystal and Molecular Structures Program for Mac and Windows*; CrystalMaker Software, Ltd., Oxford, England (www.crystalmaker.com).

(8) Phillips, T. L.; Loveless, J. K.; Bailey, S. W. Cr^{3+} coordination in chlorites: A structural study of ten chromian chlorites. *Am. Mineral.* **1980**, *65*, 112−122.

(9) *Inorganic Crystal Structure Database (ICSD)*. http://icsd.cds.rsc.org/; accessed Sept. 1, 2018.

(10) Bower, W. R.; Smith, A. D.; Pattrick, R. A.; Pimblott, S. M. Note: Establishing alpha-particle radiation damage experiments using the Dalton Cumbrian Facility's 5 MV tandem pelletron. *Rev. Sci. Instrum.* **2015**, *86* (4), 046105.

(11) Leay, L.; Bower, W. R.; Horne, G.; Wady, P.; Baidak, A.; Pottinger, M.; Nancekievill, M.; Smith, A.; Watson, S.; Green, P.; Lennox, B.; LaVerne, J. A.; Pimblott, S. M. Development of irradiation capabilities to address the challenges of the nuclear industry. *Nucl. Instrum. Methods Phys. Res., Sect. B* **2015**, *343*, 62−69.

(12) Bower, W. R.; Pearce, C. I.; Smith, A.; Pimblott, S. M.; Mosselmans, J. F. W.; Haigh, S.; McKinley, J. P.; Pattrick, R. A. D. Radiation damage in biotite mica by accelerated α-particles: A synchrotron microfocus X-ray diffraction and X-ray absorption spectroscopy study. *Am. Mineral.* **2016**, *101* (4), 928−942.

(13) Ziegler, J. F.; Ziegler, M. D.; Biersack, J. P. SRIM- The stopping and range of ions in matter. *Nucl. Instrum. Methods Phys. Res., Sect. B* **2010**, *268* (11−12), 1818−1823.

(14) Meldrum, A.; Boatner, L. A.; Weber, W. J.; Ewing, R. C. Radiation damage in zircon and monazite. *Geochim. Cosmochim. Acta* **1998**, *62* (14), 2509−2520.

DOI: 10.1021/acsearthspacechem.8b00205
ACS Earth Space Chem. 2019, 3, 652−662

(15) Pattrick, R. A. D.; Charnock, J. M.; Geraki, T.; Mosselmans, J. F. W.; Pearce, C. I.; Pimblott, S. M.; Droop, G. T. R. Alpha particle damage in biotite characterized by microfocus X-ray diffraction and Fe K-edge X-ray absorption spectroscopy. *Mineral. Mag.* **2013**, *77* (6), 2867−2882.
(16) Stadelmann, P. *JEMS-SAAS V4.0*. Available via the Internet at: http://www.jems-saas.ch/Home/jemsWebSite/jems.html; accessed March 1, 2015.
(17) Ilavsky, J. *Nika Package for 2D → 1D SAS data reduction V1.18*. Available via the Internet at: https://usaxs.xray.aps.anl.gov/software/nika; accessed March 1, 2015.
(18) Basham, M.; Filik, J.; Wharmby, M. T.; Chang, P. C.; El Kassaby, B.; Gerring, M.; Aishima, J.; Levik, K.; Pulford, B. C.; Sikharulidze, I.; Sneddon, D.; Webber, M.; Dhesi, S. S.; Maccherozzi, F.; Svensson, O.; Brockhauser, S.; Naray, G.; Ashton, A. W. Data Analysis WorkbeNch (DAWN). *J. Synchrotron Radiat.* **2015**, *22* (3), 853−858.
(19) Filik, J.; Ashton, A. W.; Chang, P. C. Y.; Chater, P. A.; Day, S. J.; Drakopoulos, M.; Gerring, M. W.; Hart, M. L.; Magdysyuk, O. V.; Michalik, S.; Smith, A.; Tang, C. C.; Terrill, N. J.; Wharmby, M. T.; Wilhelm, H. Processing two-dimensional X-ray diffraction and small-angle scattering data in DAWN 2. *J. Appl. Crystallogr.* **2017**, *50*, 959−966.
(20) Ravel, B.; Newville, M. ATHENA, ARTEMIS, HEPHAESTUS: data analysis for X-ray absorption spectroscopy using IFEFFIT. *J. Synchrotron Radiat.* **2005**, *12*, 537−541.
(21) *XAFS Spectra Library*. Available via the Internet at: http://cars.uchicago.edu/xaslib/about/; accessed Feb. 1, 2019.
(22) Wilke, M.; Farges, F.; Petit, P.-E.; Brown, G. E. J.; Martin, F. Oxidation state and coordination of Fe in minerals: An Fe K-XANES spectroscopic study. *Am. Mineral.* **2001**, *86*, 714−730.
(23) Prieto, A. C.; Dubessy, J.; Cathelineau, M. Structure-composition relationships in trioctahedral chlorites: a vibrational spectroscopy study. *Clays Clay Miner.* **1991**, *39* (5), 531−539.
(24) Coates, J. Interpretation of Infrared Spectra: A Practical Approach. In *Encyclopedia of Analytical Chemistry*; Meyers, R. A., Ed.; John Wiley & Sons, Ltd.: 2000.
(25) Fleet, M. E.; Deer, W. A.; Howie, R. A.; Zussman, J. In *Micas*; Rock-Forming Minerals, Vol. *3A*; Geological Society: London, 2003; p 765.
(26) Grygar, T.; Bezdicka, P.; Hradil, D.; Hruskova, M.; Novotna, K.; Kadlec, J.; Pruner, P.; Oberhansli, H. Characterisation of expandable clay minerals in Lake Baikal sediments by thermal dehydration and cation exchange. *Clays Clay Miner.* **2005**, *53*, 389−400.
(27) Ilton, E. S.; Heald, S. M.; Smith, S. C.; Elbert, D.; Liu, C. Reduction of uranyl in the interlayer region of low iron micas under anoxic and aerobic conditions. *Environ. Sci. Technol.* **2006**, *40*, 5003−5009.
(28) Fuller, A. J.; Shaw, S.; Ward, M. B.; Haigh, S. J.; Mosselmans, J. F. W.; Peacock, C. L.; Stackhouse, S.; Dent, A. j.; Trivedi, D.; Burke, I. T. Caesium incorporation and retention in Illite interlayers. *Appl. Clay Sci.* **2015**, *108*, 128−134.
(29) Chisholm-Brause, C.; Conradson, S. D.; Buscher, C. T.; Eller, P. G.; Morris, D. E. Speciation of uranyl sorbed at multiple binding sites on montmorillonite. *Geochim. Cosmochim. Acta* **1994**, *58*, 3625−3631.
(30) McKinley, J. P.; Zachara, J. M.; Smith, S. C.; Turner, G. D. The influence of uranyl hydrolysis and multiple site-binding reactions of adsorption of UVI to montmorillonite. *Clays Clay Miner.* **1995**, *43*, 586−598.
(31) Hennig, C.; Reich, T.; Dahn, R.; Scheidegger, A. M. Structure of uranium sorption complexes at montmorillonite edge sites. *Radiochim. Acta* **2002**, *90*, 653−657.
(32) Begg, J.; Zavarin, M.; Zhao, P.; Tumey, S. J.; Powell, B.; Kersting, A. B. Pu(V) and Pu(IV) sorption to montmorillonite. *Environ. Sci. Technol.* **2013**, *47* (10), 5146−5153.
(33) Ilton, E. S.; Haiduc, A.; Cahill, C. L.; Felmy, A. R. Mica surfaces stabilize pentavalent uranium. *Inorg. Chem.* **2005**, *44* (9), 2986−2988.
(34) Tsarev, S.; Waite, T. D.; Collins, R. N. Uranium Reduction by Fe(II) in the Presence of Montmorillonite and Nontronite. *Environ. Sci. Technol.* **2016**, *50* (15), 8223−8230.
(35) Chakraborty, S.; Favre, F.; Banerjee, D.; Scheinost, A. C.; Mullet, M.; Ehrhardt, J. J.; Brendle, J.; Vidal, L.; Charlet, L. U(VI) sorption and reduction by Fe(II) sorbed on montmorillonite. *Environ. Sci. Technol.* **2010**, *44* (10), 3779−3785.
(36) Pabalan, R. T.; Turner, D. R. Uranium(6+) sorption on montmorillonite: Experimental and surface complexation modeling study. *Aquat. Geochem.* **1996**, *2* (3), 203−226.
(37) Brookshaw, D. R.; Lloyd, J. R.; Vaughan, D. J.; Pattrick, R. A. D. Effects of microbial Fe(III) reduction on the sorption of Cs and Sr on biotite and chlorite. *Geomicrobiol. J.* **2016**, *33* (3−4), 206−215.

DOI: 10.1021/acsearthspacechem.8b00205
ACS Earth Space Chem. 2019, 3, 652−662